

Electronic structure and spin-lattice relaxation in superconducting vortex states on the kagome lattice near van Hove filling

Hong-Min Jiang,¹ Shun-Li Yu,² and Xiao-Yin Pan³

¹*School of Science, Zhejiang University of Science and Technology, Hangzhou 310023, China*

²*National Laboratory of Solid State Microstructures and Department of Physics, Nanjing University, Nanjing 210093, China*

³*Department of Physics, Ningbo University, Ningbo 315211, China*

(Dated: February 11, 2022)

Starting from a tight-binding model on the kagome lattice near the van Hove filling, the superconducting (SC) properties are investigated self-consistently using the Bogoliubov-de Gennes equation with the consideration of the inequivalent third-neighbor (TN) bonds. Near the van Hove filling, the most favorable SC pairings are found to derive from the electrons belonging to the same sublattice sites, including the on-site s -wave and the spin-singlet/triplet TN pairings. The inequivalent TN bonds will result in multiple SC components with different orbital angular momentums (OAM) for the TN SC pairings. While the density of states (DOS) and the temperature (T) dependence of the spin-lattice relaxation rate (T_1^{-1}) exhibit distinct line shapes in the SC state for the three cases, a peak structure in the T dependence of T_1^{-1} can be found for both cases just below T_c as a result of the van Hove singularity, even though the SC gap has nodes. The effects of magnetic vortices on the low energy excitations and on the T dependence of T_1^{-1} with the implications of the results are also discussed for both cases.

PACS numbers:

Recently, much attention has been focused on superconductivity in a family of compounds AV_3Sb_5 ($A=K, Rb,$ and Cs)^{1–35}, which share a common lattice structure with kagome net of vanadium atoms. Materials based on kagome lattices have been predicted to host exotic quantum physics because they embrace the geometrical lattice frustration, the flat electronic bands, the Dirac cones and the topologically nontrivial surface states. Meanwhile, the SC phase appears next to a charge density wave phase in the pressure-temperature phase diagram. As the electrons in these materials suffer simultaneously from the geometrical frustration, topological band structure and the competition between different possible ground states, the observations of the superconductivity in these topological metals are in themselves exotic and rare. The connection to the underlying lattice geometry and the topological nature of the band structure further places them in the context of wider research efforts in topological physics and superconductivity.

To understand the underlying mechanism of the superconductivity in kagome superconductors and its connection to the lattice geometry and the topological nature of the band structure, numerous experiments with various means were conducted in the past two years. However, the inconsistent or even contradicting results were found so far in experimental measurements and data analysis. The temperature dependence of the nuclear spin-lattice relaxation rate shows a Hebel-Slichter coherence peak just below T_c , indicating that CsV_3Sb_5 is a nodeless s -wave superconductor¹⁴. The penetration depth measurements also claim a nodeless gap¹⁵. Nevertheless, recent measurements of thermal conductivity on CsV_3Sb_5 at ultra-low temperature evidenced a finite residual linear term, pointing to an unconventional nodal SC¹⁶. In accordance with this, the V-shaped SC gaps with residual

zero-energy density of states also suggest an anisotropic SC gap with nodes^{11–13}. Moreover, the STM experiment on CsV_3Sb_5 at ultra-low temperature revealed a two-gap structure with multiple sets of coherent peaks and residual zero-energy DOS, accompanied by the magnetic/non-magnetic impurity effect, implying a rather novel and interesting SC gap, i.e., the sign preserved multiband superconductivity with gap nodes¹².

On the theoretical side, the vicinity to the van Hove filling was proposed to be crucial to the superconductivity on the kagome lattice. By using the variational cluster approach, the chiral $d_{x^2-y^2} + id_{xy}$ -wave SC state was found to be the most favorable within a reasonable parameter range for the van Hove filling kagome system based on the single-orbital Hubbard model with the 1/6 hole doping³⁶. Moreover, in Ref. 36, the sublattice character of the Bloch state on the Fermi surface (FS) was shown to play a vital role in determining the superconductivity of the kagome system, which was also emphasized in the subsequent functional renormalization group (FRG) studies^{37–39}. By considering the extended short-range interactions, the FRG studies on kagome systems discovered a rich variety of electron instability, including magnetism, charge order as well as superconductivity near the van Hove filling^{37–39}. More recently, a random phase approximation based on a two-orbital model revealed a f -wave pairing instability over a large range of coupling strength, succeeded by d -wave singlet pairing for stronger coupling⁴⁰. Further more, it has been shown that the coexistence of time-reversal symmetry breaking with a conventional fully gapped superconductivity could lead to the gapless excitations on the domains of the lattice symmetry breaking order⁴¹. The chiral flux phase has also been proposed to explain time-reversal symmetry breaking in the kagome superconductors^{42,43}.

In view of the divergent experimental observations and the various theoretical predictions, it is highly demanded to compare the consequences of the theoretical predictions on the experimental observations, especially with the emphases on the roles played by the van Hove singularity and the inequivalent bonds on the kagome lattice in a single-orbital Hubbard description. In this paper, we carry out such an investigation on the SC pairing symmetries of the kagome superconductors and compare their consequences on the experimental observations. The study is to some extent an extension to Ref. 36 by incorporation of the three inequivalent TN bonds on the kagome lattice. Starting from a single-orbital tight-binding model on the kagome lattice near the van Hove singularity at 1/6 hole doping, the mean-field calculations demonstrate that the most favorable SC pairings are derived from the electrons belonging to the same sublattice sites, including the on-site s -wave and the spin-singlet/triplet TNs pairings, which are in line with the variational cluster perturbation results. However, the incorporation of the inequivalent TN bonds will lead to the SC pairing with multiple OAM components with mixed $s_{ex} + (d \pm id')$ / $(p \pm ip')$ + f -wave symmetries, and thus contributes to the two-gap structures of the DOS. Although the spin-lattice relaxation exhibit distinct T dependence for the three cases, the Hebel-Slichter (or Hebel-Slichter-like) peak structure can be found for both cases just below T_c due to the Fermi level being near the van Hove singularity. In the vortex states, the cases for the on-site s -wave and the mixed $s_{ex} + (d \pm id')$ -wave pairings possess discrete in-gap state peaks, located on either side of the zero energy. Nevertheless, the near-zero-energy in-gap state peak occurs in the vortex core for the case of the mixed $(p \pm ip') + f$ -wave pairing. The vortices suppress the Hebel-Slichter (or Hebel-Slichter-like) peaks of the spin-lattice relaxation rate, but enhance them at low temperature. While a sophisticated multi-orbital model is more appropriate to make a direct comparison to the experimental results, the multiple components of the SC pairing originated from the inequivalent bonds on the kagome lattice and the Hebel-Slichter (or Hebel-Slichter-like) peak of T_1^{-1} below T_c due the vicinity to the van Hove filling are expected to persist in a realistic multi-orbital description and should be reflected in the experimental observations, provided that the system situates close to the van Hove filling and the SC pairing is nonlocal.

The effective electron hoppings on a kagome lattice can be described by the following tight-binding Hamiltonian,

$$H_0 = - \sum_{\langle ij \rangle \sigma} (t_{ij} c_{i\sigma}^\dagger c_{j\sigma} + h.c.) - \mu \sum_{i\sigma} c_{i\sigma}^\dagger c_{i\sigma}, \quad (1)$$

where $c_{i\sigma}^\dagger$ creates an electron with spin σ on the site \mathbf{r}_i of the kagome lattice and $\langle ij \rangle$ denotes nearest-neighbors (NN). t_{ij} is the hopping integral between the NN sites, and μ the chemical potential. For the free hopping case with $t_{ij} = t$, the Hamiltonian H_0 can be written in the

momentum space,

$$H_0(k) = \sum_{k\sigma} \Psi_{k\sigma}^\dagger \mathcal{H}_k^0 \Psi_{k\sigma}, \quad (2)$$

with $\Psi_{k\sigma} = (c_{Ak\sigma}, c_{Bk\sigma}, c_{Ck\sigma})^T$ and

$$\mathcal{H}_k^0 = -2t \begin{pmatrix} 0 & \cos k_1 & \cos k_2 \\ \cos k_1 & 0 & \cos k_3 \\ \cos k_2 & \cos k_3 & 0 \end{pmatrix}. \quad (3)$$

The index $m = A, B, C$ in $c_{mk\sigma}$ labels the three basis sites in the triangular unit cell. k_n is abbreviated from $\mathbf{k} \cdot \boldsymbol{\tau}_n$ with $\tau_1 = \hat{x}/2$, $\tau_2 = (\hat{x} + \sqrt{3}\hat{y})/4$ and $\tau_3 = \tau_2 - \tau_1$ denoting the three NN vectors. The label of the sublattice sites, the NN vectors and the translational vectors are shown in Fig. 1(a). As shown in Fig. 1(c), the spectrum of \mathcal{H}_k^0 consists of one flat band $E_k^{(3)} = 2t$ and two dispersive bands

$$E_k^{(1,2)} = t(-1 \pm \sqrt{4P_k - 3}), \quad (4)$$

with $P_k = \cos^2 k_1 + \cos^2 k_2 + \cos^2 k_3$. In addition to the two inequivalent Dirac points formed by the touching points of band 1 and 2 at $\mathbf{K}_\pm = (\pm 2\pi/3, 0)$ and the touching point of band 2 and 3 at the center of the Brillouin zone (BZ), there are three van Hove singularities with one originating from the flat band, and the other two originating from the saddle points at M point of the BZ, as illustrated in Fig. 1(d). The Fermi levels at upper and lower saddle points correspond to the 1/2 and 1/6 hole doping. Near the van Hove singularity at 1/6 hole doping, the hexagonal FS shown in Fig. 1(b) is similar to the ARPES experimental observation and the DFT calculations¹, though a simple d -orbital tight-binding model was adopted. In the calculations, we focus our study on the 1/6 hole doping, as has been done in Ref. 36.

The SC pairing is assumed to derive from the effective attractions between electrons,

$$H_P = V \sum_{ij, \sigma\sigma'} n_{i, \sigma} n_{j, \sigma'}. \quad (5)$$

In the mean-field approximation, the attractions can lead to the SC pairings in the spin-singlet and spin-triplet channels respectively as,

$$H_{Ps} = \sum_{ij} (\Delta_{s,ij} c_{i,\uparrow}^\dagger c_{j,\downarrow}^\dagger + h.c.), \quad (6)$$

and

$$H_{Pt} = \sum_{ij} (\Delta_{t,ij} c_{i,\uparrow}^\dagger c_{j,\downarrow}^\dagger + h.c.), \quad (7)$$

where the spin-singlet/triplet pairing potential is defined as $\Delta_{s/t,ij} = \frac{V_s/t}{2} (\langle c_{i,\uparrow} c_{j,\downarrow} \rangle \mp \langle c_{i,\downarrow} c_{j,\uparrow} \rangle)$. Here, we consider the case of spin-triplet pairing with the \mathbf{d} -vector along the z -axis. Then, one obtains the total Hamiltonian as

$$H = H_0 + H_{Ps/t}. \quad (8)$$

Based on the Bogoliubov transformation, the diagonalization of the Hamiltonian H can be achieved by solving the following discrete BdG equations,

$$\sum_j \begin{pmatrix} H_{ij,\sigma} & \Delta_{s/t,ij} \\ \Delta_{s/t,ij}^* & -H_{ij,\bar{\sigma}}^* \end{pmatrix} \begin{pmatrix} u_{n,j,\sigma} \\ v_{n,j,\bar{\sigma}} \end{pmatrix} = E_n \begin{pmatrix} u_{n,i,\sigma} \\ v_{n,i,\bar{\sigma}} \end{pmatrix}, \quad (9)$$

where $H_{ij,\sigma} = -t_{ij}\delta_{i+\tau_j,j} - \mu\delta_{i,j}$ with τ_j denoting the four NN vectors. $u_{n,i,\sigma}$ and $v_{n,i,\bar{\sigma}}$ are the Bogoliubov quasiparticle amplitudes on the i -th site with corresponding eigenvalue E_n . The SC pairing amplitude and electron densities are obtained through the following self-consistent equations,

$$\begin{aligned} \Delta_{s/t,ij} &= \frac{V_{s/t}}{4} \sum_n (u_{n,i,\sigma} v_{n,j,\bar{\sigma}}^* \pm v_{n,i,\bar{\sigma}}^* u_{n,j,\sigma}) \times \\ &\quad \tanh\left(\frac{E_n}{2k_B T}\right) \\ n_{i,\uparrow} &= \sum_n |u_{n,i,\uparrow}|^2 f(E_n) \\ n_{i,\downarrow} &= \sum_n |v_{n,i,\downarrow}|^2 [1 - f(E_n)]. \end{aligned} \quad (10)$$

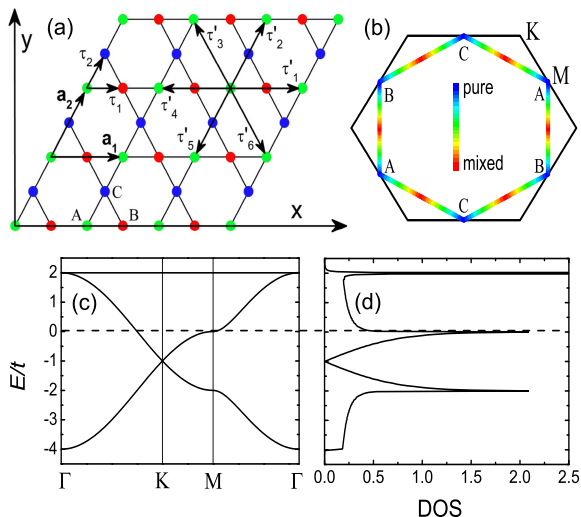


FIG. 1: (a) The lattice structure of the kagome superconductor, made out of three sublattices A (green dots), B (red dots) and C (blue dots). \mathbf{a}_1 and \mathbf{a}_2 are two translational vectors, τ_1 and τ_2 the nearest-neighbor vectors, and τ'_1 - τ'_6 the third-neighbor vectors. (b) Fermi surface and weights of the contribution to Fermi surface from three inequivalent lattice sites A , B , and C as represented by the colors. (c) The tight-binding dispersion along high-symmetry cuts. The dashed line is the Fermi level corresponding to the van Hove filling. (d) Normal state density of states.

At 1/6 hole doping, since the van Hove singularity at each saddle point M on the FS comes only from one of the three inequivalent lattice sites, as shown in Fig. 1(b), one can expect that the favorable Cooper pairings are derived from two electrons belonging to the same sublattice.

		$\Delta_{s/t,\tau'_1}$	$\Delta_{s/t,\tau'_2}$	$\Delta_{s/t,\tau'_3}$
TN spin-singlet	A site	0.05	0.05	-0.03
	B site	-0.03	0.05	0.05
	C site	0.05	-0.03	0.05
TN spin-triplet	A site	-0.04	0.04	-0.067
	B site	-0.067	0.04	-0.04
	C site	-0.04	0.067	-0.04

TABLE I: Pairing strength on the three inequivalent TN bonds for the three sublattice sites.

Therefore, we consider the on-site and the TN pairings, which are in the same sublattice. For the kagome lattice, there are six TNs for each lattice site, and they give rise to three inequivalent bonds, as denoted by τ'_1 , τ'_2 and τ'_3 in Fig. 1(a). While only spin-singlet pairing is allowed for the on-site pairing, both the spin-singlet and spin-triplet pairings are permissible for the TN bonds. Since the three bonds are different, we only set the pairing on each bond to be spin-singlet or spin-triplet, and let the pairing amplitude on the three different bonds to be determined self-consistently. For the TN pairings, we have $\Delta_{s,\tau'_4} = \pm\Delta_{s,\tau'_1}$, $\Delta_{s,\tau'_5} = \pm\Delta_{s,\tau'_2}$ and $\Delta_{s,\tau'_6} = \pm\Delta_{s,\tau'_3}$ for the spin-singlet/triplet pairings. In the calculations, we choose the effective pairing interactions $V_s = V_{s0} = 1.6$ for the on-site s -wave pairing, $V_s = V_{s1} = 1.2$ for the TN spin-singlet pairing, and $V_t = 1.4$ for the TN spin-triplet pairing respectively to give rise to the comparable SC transition temperatures for the three cases. At zero field, the self-consistent results of the TN pairing amplitudes on the three different bonds around three sublattice sites are displayed in table I.

The different pairing strengths on the three inequivalent bonds will generally lead to a SC pairing with multiple components of the orbital angular momentum. It would be useful to get some perspective on the symmetries of the TN bond SC pairings in the kagome lattice from the real space description. In real space, the pairing amplitude on site \mathbf{r}_i is generally defined as,

$$\Delta_{s/t,+/-}^l(\mathbf{r}_i) = \frac{1}{N_c} \sum_{\tau'_j} \Delta_{s/t,\tau'_j} e^{il\theta_{+/-}(\tau'_j)}. \quad (11)$$

Here, $\Delta_{s/t,+/-}^l(\mathbf{r}_i)$ stands for the clockwise/anticlockwise (+/-) spin-singlet/triplet (s/t) pairing with orbital momentum l in unit of \hbar , which determines the spatial symmetry of the Cooper pair wavefunction. $\theta_{+/-}(\tau'_j)$ denotes the polar angle of the TN bond measured anticlockwise/clockwise from the x -axis, and N_c is the number of the TN sites around \mathbf{r}_i . In Eq. (11), $\Delta_{s/t,+/-}^l(\mathbf{r}_i)$ with $l = 0, 1, 2, 3, \dots$ picks up respectively the orbital components of s, p, d, f, \dots -waves, and the relationship between $\Delta_{s/t,+}^l(\mathbf{r}_i)$ and $\Delta_{s/t,-}^l(\mathbf{r}_i)$ tells us the information about the pairing chirality. From Eq. (11) and the self-consistent results shown in table I, one could get mixed $s_{ex} + (d \pm id')$ -wave symmetry for the TN spin-singlet

pairing and mixed ($p \pm ip'$) + f -wave symmetry for the TN spin-triplet pairing. In reciprocal space, the components with different orbital momentums have the following form,

$$\begin{aligned}\Delta_{s_{ex}}(\mathbf{k}) &= \Delta_0^{s_{ex}} [\cos(k_x) + 2 \cos(k_x/2) \cos(\sqrt{3}k_y/2)]; \\ \Delta_{d \pm id'}(\mathbf{k}) &= \Delta_0^{d \pm id'} [\cos(k_x) - \cos(k_x/2) \cos(\sqrt{3}k_y/2) \\ &\quad \pm i\sqrt{3} \sin(k_x/2) \sin(\sqrt{3}k_y/2)]; \\ \Delta_{p \pm ip'}(\mathbf{k}) &= \Delta_0^{p \pm ip'} [\sin(k_x) + \sin(k_x/2) \cos(\sqrt{3}k_y/2) \\ &\quad \pm i\sqrt{3} \cos(k_x/2) \sin(\sqrt{3}k_y/2)]; \\ \Delta_f(\mathbf{k}) &= \Delta_0^f [\sin(k_x) - 2 \sin(k_x/2) \cos(\sqrt{3}k_y/2)]\end{aligned}\quad (12)$$

where $\Delta_0^{s_{ex}} = |\Delta_s^0|$, $\Delta_0^{d \pm id'} = |\Delta_{s,\pm}^2|$, $\Delta_0^{p \pm ip'} = |\Delta_{t,\pm}^1|$ and $\Delta_0^f = |\Delta_t^3|$. The values of the s_{ex}/f -wave $\Delta_0^{s_{ex}}/\Delta_0^f$ and the $d \pm id'/p \pm ip'$ -wave components $\Delta_0^{d \pm id'}/\Delta_0^{p \pm ip'}$ are shown in table II, and the sign distributions of the pairing components refer to Ref. 36 for details. While the s_{ex} - and $d \pm id'$ -waves components exhibit comparable strength for the TN spin-singlet pairing, the f -wave component dominates over the $p \pm ip'$ -wave component for the TN spin-triplet pairing. The smallness of the $p \pm ip'$ -wave component in the mixed ($p \pm ip'$) + f -wave symmetry pairing state will not remove the nodes of the f -wave pairing but will move them, resulting in an unusual SC pairing state with accidental nodes. The equality of $\Delta_0^{d \pm id'/p \pm ip'}$ and $\Delta_0^{d - id'/p - ip'}$ dictates the two degenerate SC pairing states with right and left chiralities in the $d \pm id'/p \pm ip'$ -wave component at zero field.

The three typical SC parings in their uniform SC states produce distinct site-averaged DOS spectra $N(E) = \frac{1}{N} \sum_i N(E, \mathbf{r}_i)$ with definition $N(E, \mathbf{r}_i) = N_{\uparrow}(E, \mathbf{r}_i) + N_{\downarrow}(E, \mathbf{r}_i) = -\sum_n [|u_{i,\uparrow}^n|^2 f'(E_n - E) + |v_{i,\downarrow}^n|^2 f'(E_n + E)]$, which is proportional to the differential tunneling conductance observed in scanning tunneling microscopy (STM) experiments. The results are summarized by the solid black lines at the bottom of each panels in Fig. 3. For the on-site s -wave symmetry, a single U-shaped full gap structure can be seen in the DOS as shown by the solid black line in Fig. 3(a), depicting a typical feature for the isotropic SC gap without nodes along the FS. In the $s_{ex} + (d \pm id')$ -wave symmetry, the DOS consists of a small U-shaped gap structure at low energy and a broad V-shaped gap structure at higher energy as shown in Fig. 3(b), presenting an anisotropic nodeless two-gap structure. As for the ($p \pm ip'$) + f -wave symmetry shown in Fig. 3(c), dominant f -wave component plus a tiny value of $p \pm ip'$ -wave component produce a broad V-shaped gap structure inlaid by a small V-shaped gap with residual DOS at zero energy in the SC state, displaying a characteristic of nodal two-gap SC pairing. We note that the V-shaped SC gap with multiple sets of coherent peaks and residual zero-energy DOS are in good accordance with the STM experiments¹¹⁻¹³.

Now we address the vortex structure of the three types of the SC states. In the presence of a perpendicular magnetic field, the hopping terms are described

	$\Delta_0^{s_{ex}/f}$	$\Delta_0^{d+id'/p+ip'}$	$\Delta_0^{d-id'/p-ip'}$
TN spin-singlet	0.023	0.027	0.027
TN spin-triplet	0.049	0.009	0.009

TABLE II: Pairing amplitude for the different orbital components.

by the Peierls substitution. For the NN hopping between sites i and $i + \tau_j$, one has $t_{i,i+\tau_j} = t e^{i\varphi_{i,i+\tau_j}}$, where $\varphi_{i,i+\tau_j}(\tau_j) = \frac{\pi}{\Phi_0} \int_{r_{i+\tau_j}(\tau_j)}^{r_i} \mathbf{A}(\mathbf{r}) \cdot d\mathbf{r}$ with $\Phi_0 = \frac{hc}{2e}$ being the SC flux quanta. In this case, the pairing amplitude on site \mathbf{r}_i is reformulated as $\Delta_{s/t,L/R}^l(\mathbf{r}_i) = \frac{1}{N_c} \sum_{\tau_j} \Delta_{s/t,\tau_j} e^{i\theta_{R/L}(\tau_j)} e^{i\varphi_{i,i+\tau_j}}$. In the calculations, we consider a parallelogram vortex unit cell with size of $22\mathbf{a}_1 \times 44\mathbf{a}_2$ as shown in Fig. 1(a), where two vortices are accommodated. The vector potential $\mathbf{A}(\mathbf{r}) = (0, Bx, 0)$ is chosen in the Landau gauge to give rise to the magnetic field \mathbf{B} along the z -direction.

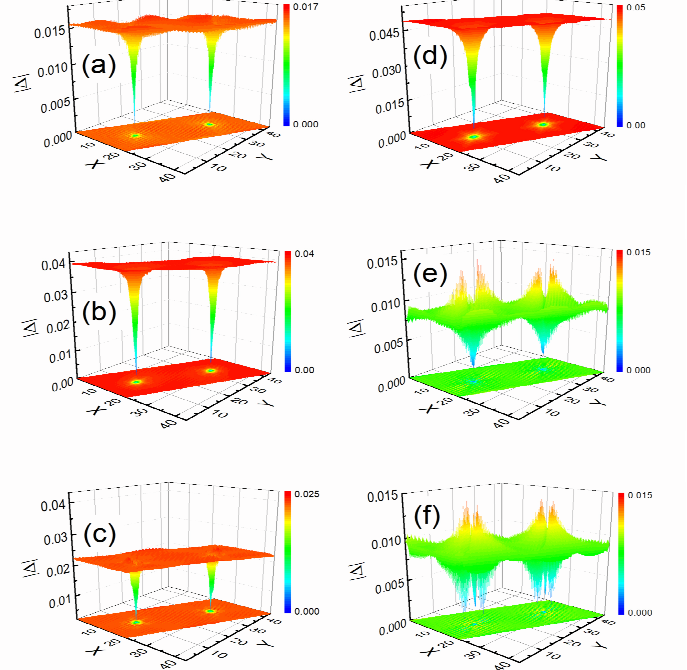


FIG. 2: The spatial distributions of the SC order parameters in the vortex states for the mixed $s_{ex} + (d \pm id')$ - (left panel), and ($p \pm ip'$) + f -wave (right panel) symmetries. (a), (b) and (c) show the spatial distributions of the amplitudes for the s_{ex} , $d + id'$ and $d - id'$ components, respectively. (d), (e) and (f) show the spatial distributions of the amplitudes for the f , $p + ip'$ and $p - ip'$ components, respectively.

Under a perpendicular magnetic field, the vanishment of the screening current density at the vortex center

drives the system into the vortex states with the suppression of the SC order parameter around the vortex core, thereby forming a vortex with winding +1. In the vortex states, the SC order parameter $|\Delta(\mathbf{r}_i)|$ vanishes at the vortex core center and recovers its bulk value at the core edge with the core size ξ_1 on the scale of coherent length ξ_0 , as can be seen from Fig. 3 for both cases (The case of on-site s -wave pairing is not shown here). Besides the standard SC vortex structure, there are two prominent features to be specified in the vortex states for the SC pairings with multiple OAM components on the kagome lattice. Firstly, consistent with the STM experimental observations in CsV_3Sb_5 ¹² and similar to the observations in NbSe_2 ^{44–46} and $\text{YNi}_2\text{B}_2\text{C}$ ^{47–49}, the vortex core has a typical star shape with sixfold symmetry for both cases, reflecting the underlying crystalline band structure. Secondly, the afore mentioned two degenerate SC pairing states with right and left chiralities in the $d \pm id'/p \pm ip'$ -wave component are removed under a perpendicular magnetic field, because $d \pm id'/p \pm ip'$ -wave components correspond to states with an internal phase winding of the Cooper pairs along the z -axis. In the mixed $s_{ex} + (d \pm id')$ -wave pairing state, the comparable strength for the s_{ex} - and $d \pm id'$ -wave components renders both of them to respond effectively to the magnetic field. The internal phase of the $d + id'$ -wave component has a -2 winding, which counteracts the phase winding $+1$ of the vortex to save the energy cost of supercurrents. As a result, the application of the magnetic field transfers the weight from the s_{ex} - and $d - id'$ -wave components to the $d + id'$ -wave component in the mixed $s_{ex} + (d \pm id')$ -wave pairing state, as evidenced by a comparison of table II with the spatial distributions of the SC order parameters in Figs. 2(a), 2(b) and 2(c). On the other hand, the screening current density from the dominant f -wave component in the mixed $(p \pm ip') + f$ -wave symmetry pairing diminishes the impact of the magnetic field on the $p \pm ip'$ -wave components, so there is a little degeneracy lifting for the two chiral $p \pm ip'$ -wave components as shown in Figs. 2(e) and 2(f), despite the $p - ip'$ -wave component possessing the internal phase winding -1 .

Then, we pursue the electronic structures in the vortex states by examining the energy dependence of the LDOS. In order to reduce the finite size effect, the calculations of the LDOS are carried out on a periodic lattice which consists of 16×8 parallelogram supercells, with each supercell being the size $22\mathbf{a}_1 \times 44\mathbf{a}_2$. In Fig. 3, we show the energy dependence of the LDOS on a series of sites along the long side direction of the parallelogram moving away from the core center. Since both the on-site s -wave and the mixed $s_{ex} + (d \pm id')$ -wave pairings are fully gaped, similar in-gap states appear in the core region. At the vortex center, the Caroli-de Gennes-Matricorn states at the vortex center accumulate to give rise to two peaks reside on each side about the zero energy, forming a small gap at the zero energy. As the site moving away from the vortex center, the two peaks depart further and fade away, as presented in Figs. 3(a) and 3(b). For the mixed

$(p \pm ip') + f$ -wave symmetry pairing, by contrast, a near-zero peak appears at the vortex center, which does not disperse in a large distance as moving away from the vortex center. It is worth noting that the near-zero energy peak and the dispersionless of the peak are again in excellent agreement with the STM experimental observations¹³.

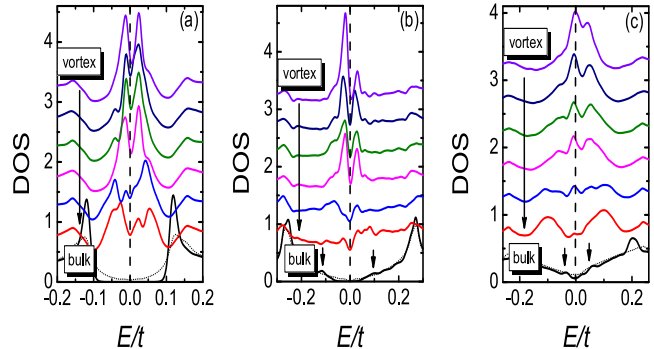


FIG. 3: The energy dependence of the LDOS on a series of sites for on-site spin-singlet pairing (a), spin-singlet pairing on the same-sublattice bond (b), and spin-triplet pairing on the same-sublattice bond (c). In each panel from top to bottom, the curves stand for the LDOS at sites along the long side direction of the parallelogram moving away from the core center. The curves are vertically shifted for clarity. At the bottom of each panels, the DOS in the uniform SC state and the site-averaged DOS in the vortex states are plotted as solid black lines and dotted black lines, respectively. The dashed vertical lines in each panel denote the position of the zero bias, and the short arrows in (b) and (c) mark the secondary gap edges.

Next, we turn to the discussion of the T dependence of T_1^{-1} . The site-dependent $T_1^{-1}(\mathbf{r}_i, \mathbf{r}_{i'})$ is given by^{50,51}

$$\begin{aligned}
 R(\mathbf{r}_i, \mathbf{r}_{i'}) &= \text{Im} \chi_{+,-}(\mathbf{r}_i, \mathbf{r}_{i'}, i\Omega_n \rightarrow \Omega + i\eta) / (\Omega/T) |_{\Omega \rightarrow 0} \\
 &= - \sum_{n,n'} [u_{n,i} u_{n,i'}^* v_{n',i} v_{n',i'}^* - v_{n,i} u_{n,i'}^* u_{n',i} v_{n',i'}^*] \\
 &\quad \times \pi T f'(E_n) \delta(E_n - E_{n'}).
 \end{aligned} \tag{13}$$

We choose $\mathbf{r}_i = \mathbf{r}_{i'}$ because the nuclear spin-lattice relaxation at a local site is dominant. Then the site-dependent relaxation time is given by $T_1(\mathbf{r}_i) = 1/R(\mathbf{r}_i, \mathbf{r}_i)$ and the bulk relaxation time $T_1 = (1/N) \sum_i T_1(\mathbf{r}_i)$. In the calculations, we adopt $\delta(E_n - E_{n'}) = \pi^{-1} \text{Im}(E_n - E_{n'} - i\eta)$ with typical value $\eta = 0.01$. In a conventional s -wave superconductor, the T dependence of T_1^{-1} develops a peak structure below T_c , which is called Hebel-Slichter coherence peak as observed experimentally in SC Al by Hebel and Slichter⁵², and explained theoretically as a result of the enhancement of the SC DOS at the gap edge along with the non-zero coherent factor described in BCS theory⁵². Thus the observation of the Hebel-Slichter peak below T_c is usually considered to be the hallmark for s -wave superconductivity¹⁴.

In the absence of the magnetic field, the Hebel-Slichter (or Hebel-Slichter-like) peaks of T_1^{-1} below T_c are evidenced in Figs. 4(a)-(c) for both cases. It is quite remarkable for the case of the mixed $(p \pm ip') + f$ -wave with nodal SC gap. To figure out the origin as well as the different nature of the peaks, we show in the same figures the temperature evolution of $R_D \equiv -\frac{1}{N} \sum_{i,n,n'} (u_{n,i} u_{n,i'}^* v_{n',i} v_{n',i'}^*) \pi T f'(E_n) \delta(E_n - E_{n'})$ and $R_C \equiv \frac{1}{N} \sum_{n,n'} (v_{n,i} u_{n,i'}^* u_{n',i} v_{n',i'}^*) \pi T f'(E_n) \delta(E_n - E_{n'})$, i.e., the contributions from the first and second terms in Eq. (12) to T_1^{-1} . R_D is proportional to $N_\uparrow \times N_\downarrow$, which gives rise to the enhancement of the SC DOS at the gap edge with the enhancement depending upon the sharpness of the SC gap edge and the specific DOS of the normal state on where the SC gap opens. On the other hand, R_C describes the coherent effect of the SC state. As is seen in Fig. 4(c) and the insets of Figs. 4(a) and (b), the temperature evolutions of R_D develop a peak just below T_c for both cases (Note that only R_D contributes to T_1^{-1} , and accordingly $R_D = T_1^{-1}$ for the mixed $(p \pm ip') + f$ -wave pairing, as will be shown in the following.), due to the fact that the infinitesimal SC gaps opening at the van Hove singularity with divergent DOS would also have divergent DOSs at the gap edges. However, the T dependence of R_C is different for the three cases. Specifically, R_C evolves a peak below T_c for the cases of the on-site s - and the mixed $s_{ex} + (d \pm id')$ -wave symmetries, whereas it remains zero for the case of the mixed $(p \pm ip') + f$ -wave symmetry. This can be understood by noting that the mixed triplet $(p \pm ip') + f$ -wave pairing with odd parity $\Delta_{ji} = -\Delta_{ij}$ forbids the local SC correlation $u_{n,i} v_{n,i}^*$.

Thus far, we have demonstrated that the results for the mixed $(p \pm ip') + f$ -wave symmetry reconcile the various inconsistent or apparently contradicting experiments, including the V-shaped SC gap with residual DOS at zero energy, the dispersionless of the near-zero energy peak in the vortex core, as well as the Hebel-Slichter-like peak of the T dependence of T_1^{-1} . While the appearance of the Hebel-Slichter-like peak for the mixed $(p \pm ip') + f$ -wave symmetry here seems to support the NMR experiment, its origin is different in nature from the Hebel-Slichter coherent peak. The Hebel-Slichter coherent peak for the on-site s - and the mixed $s_{ex} + (d \pm id')$ -wave pairing symmetries derives from the simultaneous enhancement of R_D and R_C , but the peak for the case of the mixed $(p \pm ip') + f$ -wave symmetry originates merely from the enhancement of R_D . Due to the nodal SC gap of the mixed $(p \pm ip') + f$ -wave pairing, the sharpness of the SC gap edge is weakened as the Fermi level deviating from the van Hove singularity, and this in turn undermines the Hebel-Slichter-like peak for the case of the mixed $(p \pm ip') + f$ -wave symmetry. As a result, the Hebel-Slichter-like peak for the case of the mixed $(p \pm ip') + f$ -wave symmetry diminishes and eventually disappears with the Fermi level deviation from the van Hove filling. This is verified in the inset of Fig. 4(c) for a specified doping level 1/7. By contrast, the Hebel-Slichter peak remains robust for the cases of the on-site s -

and the mixed $s_{ex} + (d \pm id')$ -wave pairing symmetries. To verify or falsify the above scenario, the NMR experiments on different doping levels are encouraged to observe the doping evolutions of the Hebel-Slichter-like peak.

Below T_c , the three cases, however, exhibit distinct T dependence of T_1^{-1} . The on-site s -wave pairing evolves into an exponential dependence below T_c , as presented by the solid line in Fig. 4(d), which is the consequence of the full-gaped DOS in Fig. 3(a). The gap anisotropy of the mixed $s_{ex} + (d \pm id')$ -wave pairing changes the exponential dependence to a power law relation $T_1^{-1} \sim T^\alpha$ with α varying from 4 to 5 below T_c and $T_1^{-1} \sim T^7$ at low temperature, as displayed by the solid line in Fig. 4(e). For the case of $(p \pm ip') + f$ -wave symmetry pairing, the T dependence of T_1^{-1} changes its line-shape further to $T_1^{-1} \sim T^{2.5}$ below T_c and $T_1^{-1} \sim T^{1.5}$ at low temperature, shown in Fig. 4(f), as a result of the V-shaped gap and the residual DOS at zero energy.

In the presence of the perpendicular magnetic field, on one hand, the intensity of the Hebel-Slichter (or Hebel-Slichter-like) peaks are suppressed by localized excitations within the vortex cores^{50,53}. While strong depression of the peak of R_C below T_c can be seen for the case of the on-site s -wave pairing [see the inset of Fig. 4(a)], the depression is just moderate with the peak position shifting slightly toward higher temperature for the mixed $s_{ex} + (d \pm id')$ -wave pairing symmetry [the inset of Fig. 4(b)], owing to the offsetting effect of the internal phase of the $d + id'$ -wave component [see Fig. 2(b)]. As a result, one could barely see a trail of the peak as shown by the dotted black line in Fig. 4(a) for the on-site s -wave pairing symmetry, but still evidence a robust peak feature with its position moving slightly to higher temperature for the mixed $s_{ex} + (d \pm id')$ -wave pairing symmetry [refer to the dotted black line in Fig. 4(b)]. Nevertheless, the peak of R_D below T_c is suppressed completely for both cases, due to the blunting of the gap edges as shown by the dotted black lines in Figs. 4(a)-(c). This directly leads to the disappearance of the Hebel-Slichter-like peak for the case of the mixed $(p \pm ip') + f$ -wave symmetry, as presented by the dotted line in Fig. 4(c). On the other hand, the main effect of the vortices is to enhance the T dependence of T_1^{-1} for all symmetries at low temperature. The enhancement of T_1^{-1} is exemplified in Fig. 4(a) by changing the exponential T dependence to roughly T^3 below T_c , despite little variations, for the on-site s -wave symmetry. Due to the anisotropic SC gap for the mixed $s_{ex} + (d \pm id')$ -wave pairing symmetry and the nodal SC gap for the mixed $(p \pm ip') + f$ -wave symmetry [see the dotted black lines in Fig. 3(b) and 3(c)], the enhancement becomes more pronounced in a T^β power law below T_c and $T^{\beta-1}$ at lower temperature with $\beta = 3$ for the mixed $s_{ex} + (d \pm id')$ -wave pairing symmetry and $\beta = 2$ for the the mixed $(p \pm ip') + f$ -wave symmetry, as denoted by the dotted lines in Figs. 4(e) and 4(f), respectively.

In summary, we have provided a contrastive study on the kagome superconductors at the van Hove filling with the incorporation of the inequivalent TN bonds. Al-

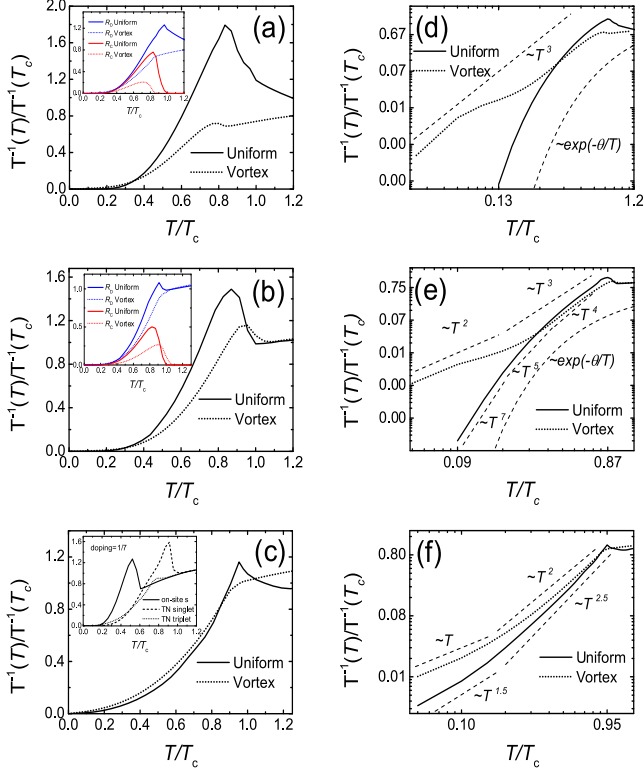


FIG. 4: Left panels: T -dependence of $\Delta(T)$ and T_1^{-1} . Right panels: T -dependence of T_1^{-1} shown in the double logarithmic chart. (a) and (d) show the results for the on-site pairing, (b) and (e) the results for the spin-singlet pairing on the TN bond, and (c) and (f) the results for the spin-triplet pairing on the TN bond. Insets in (a) and (b) display the T evolutions of R_D and R_C (see text). Inset in (c) gives the results of T dependence of T_1^{-1} for the three cases at doping $1/7$.

though the most favorable SC pairings were derived from the electrons belonging to the same sublattice sites, the consideration of the inequivalent TN bonds would result in the SC pairings with multiple OAM components, and thus contributed to the two-gap structures of the DOS. While the spin-lattice relaxation exhibited distinct T dependence in the SC state for the three cases, a peak structure has been found for both cases just below T_c .

Unlike the coherent peak for the cases of the on-site s - and the mixed $s_{ex} + (d \pm id')$ -wave pairings, which was derived from both the enhancement of the SC DOS at the gap edge and the non-zero SC coherent effect, the van Hove singularity was crucial to the peak in the mixed $(p \pm ip') + f$ -wave pairing, where only the enhancement of the SC DOS at the gap edge contributed to the peak structure. In the vortex states, the cases for the on-site s -wave and the mixed $s_{ex} + (d \pm id')$ -wave pairings created discrete in-gap state peaks, which located on either side of the zero energy. By contrast, the near-zero-energy and almost dispersionless in-gap state peak occurred in the vortex core for the case of the mixed $(p \pm ip') + f$ -wave pairing. Whereas the vortices diminished the Hebel-Slichter (or Hebel-Slichter-like) peaks and enhanced the T dependence of T_1^{-1} in the SC state for both cases, the T dependencies of T_1^{-1} were also distinct with respect to the different gap functions. While a more sophisticated multi-orbital model is needed to make a direct comparison to the experimental results, the SC pairing with multiple OAM components originated from the inequivalent bonds on the kagome lattice and the Hebel-Slichter (or Hebel-Slichter-like) peak of T_1^{-1} below T_c due the vicinity to the van Hove filling were expected to persist in a realistic multi-orbital description and should be reflected in the experimental observations, provided that the system situates close to the van Hove filling and the SC pairing is nonlocal. The NMR experiments on different doping levels and on the T dependence of the T_1^{-1} in the SC state both with and without a perpendicular magnetic field were expected to testify the theory.

note added.—After completion of this study, we become aware of recent interesting study on the vortex states in the kagome superconductors by using the similar tight-binding model⁵⁴. The SC vortex was simulated in Ref. 54 by setting the spatial dependent pairing amplitude $\Delta(\mathbf{r}_i) = \Delta \tanh(\frac{\mathbf{r}_i}{\xi})$, while the results in our study were determined self-consistently.

The authors thank Professor Jian-Xin Li for fruitful discussions and valuable suggestions. This work was supported by the National Natural Science Foundation of China (Grant Nos. 11574069, 12074175) and the K. C. Wong Magna Foundation in Ningbo University.

¹ B. R. Ortiz, S. M. L. Teicher, Y. Hu, J. L. Zuo, P. M. Sarte, E. C. Schueller, A. M. M. Abeykoon, M. J. Krogstad, S. Rosenkranz, R. Osborn, R. Seshadri, L. Balents, J. He, and S. D. Wilson, Phys. Rev. Lett. **125**, 247002 (2020).
² B. R. Ortiz, P. M. Sarte, E. M. Kenney, M. J. Graf, S. M. L. Teicher, R. Seshadri, and S. D. Wilson, Phys. Rev. Mater. **5**, 034801 (2021).
³ Q. Yin, Z. Tu, C. Gong, Y. Fu, S. Yan, and H. Lei, Chin. Phys. Lett. **38**, 037403 (2021).
⁴ K. Y. Chen, N. N. Wang, Q. W. Yin, Y. H. Gu, K. Jiang, Z. J. Tu, C. S. Gong, Y. Uwatoko, J. P. Sun, H. C. Lei,

J. P. Hu, and J.-G. Cheng, Phys. Rev. Lett. **126**, 247001 (2021).

⁵ Y. Wang, S. Yang, P. K. Sivakumar, B. R. Ortiz, S. M. L. Teicher, H. Wu, A. K. Srivastava, C. Garg, D. Liu, S. S. P. Parkin, E. S. Toberer, T. McQueen, S. D. Wilson, and M. N. Ali, arXiv:2012.05898.

⁶ Z. Zhang, Z. Chen, Y. Zhou, Y. Yuan, S. Wang, J. Wang, H. Yang, C. An, L. Zhang, X. Zhu, Y. Zhou, X. Chen, J. Zhou, and Z. Yang, Phys. Rev. B **103**, 224513 (2021).

⁷ Y.-X. Jiang, J.-X. Yin, M. M. Denner, N. Shumiya, B. R. Ortiz, G. Xu, Z. Guguchia, J. He, M. S. Hossain, X. Liu,

- J. Ruff, L. Kautzsch, S. S. Zhang, G. Chang, I. Belopolski, Q. Zhang, T. A. Cochran, D. Multer, M. Litskevich, Z.-J. Cheng, X. P. Yang, Z. Wang, R. Thomale, T. Neupert, S. D. Wilson, and M. Z. Hasan, *Nat. Mater.* **20**, 1353 (2021).
- ⁸ F. H. Yu, T. Wu, Z. Y. Wang, B. Lei, W. Z. Zhuo, J. J. Ying, and X. H. Chen, *Phys. Rev. B* **104**, L041103 (2021).
- ⁹ X. Chen, X. Zhan, X. Wang, J. Deng, X.-B. Liu, X. Chen, J.-G. Guo, and X. Chen, *Chin. Phys. Lett.* **38**, 057402 (2021).
- ¹⁰ H. Zhao, H. Li, B. R. Ortiz, S. M. L. Teicher, T. Park, M. Ye, Z. Wang, L. Balents, S. D. Wilson, and I. Zeljkovic, *Nature* **599**, 216 (2021).
- ¹¹ H. Chen, H. Yang, B. Hu, Z. Zhao, J. Yuan, Y. Xing, G. Qian, Z. Huang, G. Li, Y. Ye, S. Ma, S. Ni, H. Zhang, Q. Yin, C. Gong, Z. Tu, H. Lei, H. Tan, S. Zhou, C. Shen, X. Dong, B. Yan, Z. Wang, and H.-J. Gao, *Nature* **599**, 222 (2021).
- ¹² H.-S. Xu, Y.-J. Yan, R. Yin, W. Xia, S. Fang, Z. Chen, Y. Li, W. Yang, Y. Guo, and D.-L. Feng, *Phys. Rev. Lett.* **127**, 187004 (2021).
- ¹³ Z. Liang, X. Hou, F. Zhang, W. Ma, P. Wu, Z. Zhang, F. Yu, J.-J. Ying, K. Jiang, L. Shan, Z. Wang, and X.-H. Chen, *Phys. Rev. X* **11**, 031026 (2021).
- ¹⁴ C. Mu, Q. Yin, Z. Tu, C. Gong, H. Lei, Z. Li, and J. Luo, *Chin. Phys. Lett.* **38**, 077402 (2021).
- ¹⁵ W. Duan, Z. Nie, S. Luo, F. Yu, B. R. Ortiz, L. Yin, H. Su, F. Du, A. Wang, Y. Chen, X. Lu, J. Ying, S.D. Wilson, X. Chen, Y. Song, and H. Yuan, *Sci. China-Phys. Mech. Astron.* **64**, 107462 (2021).
- ¹⁶ C. C. Zhao, L. S. Wang, W. Xia, Q. W. Yin, J. M. Ni, Y. Y. Huang, C. P. Tu, Z. C. Tao, Z. J. Tu, C. S. Gong, H. C. Lei, Y. F. Guo, X. F. Yang, and S. Y. Li, arXiv: 2102.08356.
- ¹⁷ S. Ni, S. Ma, Y. Zhang, J. Yuan, H. Yang, Z. Lu, N. Wang, J. Sun, Z. Zhao, D. Li, S. Liu, H. Zhang, H. Chen, K. Jin, J. Cheng, L. Yu, F. Zhou, X. Dong, J. Hu, H.-J. Gao, and Z. Zhao, *Chin. Phys. Lett.* **38**, 057403 (2021).
- ¹⁸ Y. Xiang, Q. Li, Y. Li, W. Xie, H. Yang, Z. Wang, Y. Yao, and H.-H. Wen, *Nat. Commun.* **12**, 6727 (2021).
- ¹⁹ K. Y. Chen, N. N. Wang, Q. W. Yin, Y. H. Gu, K. Jiang, Z. J. Tu, C. S. Gong, Y. Uwatoko, J. P. Sun, H. C. Lei, J. P. Hu, and J.-G. Cheng, *Phys. Rev. Lett.* **126**, 247001 (2021).
- ²⁰ B. R. Ortiz, S. M. L. Teicher, L. Kautzsch, P. M. Sarte, N. Ratcliff, J. Harter, J. P. C. Ruff, R. Seshadri, and S. D. Wilson, *Phys. Rev. X* **11**, 041030 (2021).
- ²¹ X. Zhou, Y. Li, X. Fan, J. Hao, Y. Dai, Z. Wang, Y. Yao, and H.-H. Wen, *Phys. Rev. B* **104**, L041101 (2021).
- ²² Z. Liu, N. Zhao, Q. Yin, C. Gong, Z. Tu, M. Li, W. Song, Z. Liu, D. Shen, Y. Huang, K. Liu, H. Lei, and S. Wang, *Phys. Rev. X* **11**, 041010 (2021).
- ²³ M. Kang, S. Fang, J.-K. Kim, B. R. Ortiz, S. H. Ryu, J. Kim, J. Yoo, G. Sangiovanni, D. D. Sante, B.-G. Park, C. Jozwiak, A. Bostwick, E. Rotenberg, E. Kaxiras, S. D. Wilson, J.-H. Park, and R. Comin, *Nat. Phys.* (2022).
- ²⁴ Y. Fu, N. Zhao, Z. Chen, Q. Yin, Z. Tu, C. Gong, C. Xi, X. Zhu, Y. Sun, K. Liu, and H. Lei, *Phys. Rev. Lett.* **127**, 207002 (2021).
- ²⁵ Y. Song, T. Ying, X. Chen, X. Han, X. Wu, A. P. Schnyder, Y. Huang, J.-g. Guo, and X. Chen, *Phys. Rev. Lett.* **127**, 237001 (2021).
- ²⁶ H. Tan, Y. Liu, Z. Wang, and B. Yan, *Phys. Rev. Lett.* **127**, 046401 (2021).
- ²⁷ N. Shumiya, Md. S. Hossain, J.-X. Yin, Y.-X. Jiang, B. R. Ortiz, H. Liu, Y. Shi, Q. Yin, H. Lei, S. S. Zhang, G. Chang, Q. Zhang, T. A. Cochran, D. Multer, M. Litskevich, Z.-J. Cheng, X. P. Yang, Z. Guguchia, S. D. Wilson, and M. Z. Hasan, *Phys. Rev. B* **104**, 035131 (2021).
- ²⁸ F. H. Yu, D. H. Ma, W. Z. Zhuo, S. Q. Liu, X. K. Wen, B. Lei, J. J. Ying, and X. H. Chen, *Nat. Commun.* **12**, 3645 (2021).
- ²⁹ L. Yin, D. Zhang, C. Chen, G. Ye, F. Yu, B. R. Ortiz, S. Luo, W. Duan, H. Su, J. Ying, S. D. Wilson, X. Chen, H. Yuan, Y. Song, and X. Lu, *Phys. Rev. B* **104**, 174507 (2021).
- ³⁰ K. Nakayama, Y. Li, T. Kato, M. Liu, Z. Wang, T. Takahashi, Y. Yao, and T. Sato *Phys. Rev. B* **104**, L161112 (2021).
- ³¹ L. Nie, K. Sun, W. Ma, D. Song, L. Zheng, Z. Liang, P. Wu, F. Yu, J. Li, M. Shan, D. Zhao, S. Li, B. Kang, Z. Wu, Y. Zhou, K. Liu, Z. Xiang, J. Ying, Z. Wang, T. Wu, and X. Chen, *Nature* (2022).
- ³² H. Luo, Q. Gao, H. Liu, Y. Gu, D. Wu, C. Yi, J. Jia, S. Wu, X. Luo, Y. Xu, L. Zhao, Q. Wang, H. Mao, G. Liu, Z. Zhu, Y. Shi, K. Jiang, J. Hu, Z. Xu, and X. J. Zhou, *Nat. Commun.* **13**, 273 (2022).
- ³³ T. Neupert, M. M. Denner, J.-X. Yin, R. Thomale, and M. Z. Hasan, *Nat. Phys.* (2022).
- ³⁴ K. Nakayama, Y. Li, T. Kato, M. Liu, Z. Wang, T. Takahashi, Y. Yao, and T. Sato, *Phys. Rev. X* **12**, 011001 (2022).
- ³⁵ H. Li, S. Wan, H. Li, Q. Li, Q. Gu, H. Yang, Y. Li, Z. Wang, Y. Yao, and H.-H. Wen, *Phys. Rev. B* **105**, 045102 (2022).
- ³⁶ S.-L. Yu and J.-X. Li, *Phys. Rev. B* **85**, 144402 (2012).
- ³⁷ M. L. Kiesel and R. Thomale, *Phys. Rev. B* **86**, 121105(R) (2012).
- ³⁸ W.-S. Wang, Z.-Z. Li, Y.-Y. Xiang, and Q.-H. Wang, *Phys. Rev. B* **87**, 115135 (2013).
- ³⁹ M. L. Kiesel, C. Platt, and R. Thomale, *Phys. Rev. Lett.* **110**, 126405 (2013).
- ⁴⁰ X. Wu, T. Schwemmer, T. Müller, A. Consiglio, G. Sangiovanni, D. Di Sante, Y. Iqbal, W. Hanke, A. P. Schnyder, M. M. Denner, M. H. Fischer, T. Neupert, and R. Thomale, *Phys. Rev. Lett.* **127**, 177001 (2021).
- ⁴¹ Y. Gu, Y. Zhang, X. Feng, K. Jiang, and J. Hu, arXiv:2108.04703.
- ⁴² X. Feng, K. Jiang, Z. Wang, and J. Hu, *Sci. Bull.* **66**, 1384 (2021).
- ⁴³ X. Feng, Y. Zhang, K. Jiang, and J. Hu, *Phys. Rev. B* **104**, 165136 (2021).
- ⁴⁴ H. F. Hess, R. B. Robinson, and J. V. Waszczak, *Phys. Rev. Lett.* **64**, 2711 (1990).
- ⁴⁵ N. Hayashi, M. Ichioka, and K. Machida, *Phys. Rev. Lett.* **77**, 4074 (1996).
- ⁴⁶ N. Hayashi, M. Ichioka, and K. Machida, *Phys. Rev. B* **56**, 9052 (1997).
- ⁴⁷ H. Nishimori, K. Uchiyama, S. Kaneko, A. Tokura, H. Takeya, K. Hirata, and N. Nishida, *J. Phys. Soc. Jpn.* **73**, 3247 (2004).
- ⁴⁸ Y. Nagai, Y. Kato, N. Hayashi, K. Yamauchi, and H. Harima, *Phys. Rev. B* **76**, 214514 (2007).
- ⁴⁹ S. Kaneko, K. Matsuba, M. Hafiz, K. Yamasaki, E. Kalizaki, N. Nishida, H. Takeya, K. Hirata, T. Kawakami, T. Mizushima, and K. Machida, *J. Phys. Soc. Jpn.* **81**, 063701 (2012).
- ⁵⁰ M. Takigawa, M. Ichioka, and K. Machida, *Phys. Rev. Lett.* **83**, 3057 (1999); *ibid.* **90**, 047001 (2003); M. Taki-

- gawa, M. Ichioka, K. Kuroki, Y. Asano, and Y. Tanaka, *ibid.* **97**, 187002 (2006).
- ⁵¹ H.-M. Jiang, J. Guo, and J.-X. Li, Phys. Rev. B **84**, 014533 (2011).
- ⁵² L. C. Hebel and C. P. Slichter, Phys. Rev. **113**, 1504 (1959).
- ⁵³ N. J. Curro, Rep. Prog. Phys. **72**, 026502 (2009).
- ⁵⁴ P. Ding, C. H. Lee, X. Wu, and R. Thomale, arXiv: 2202.00906.